Transient Vibro-Thermography and Nonlinear Resonant Modes

G. Kolappan Geetha
Department of Aerospace Engineering,
Indian Institute of Science,
Bengaluru 560012, Karnataka, India
e-mail: ganeshkg@iisc.ac.in

D. Roy Mahapatra[1]
Professor
Department of Aerospace Engineering,
Indian Institute of Science,
Bengaluru 560012, Karnataka, India
e-mail: roymahapatra@iisc.ac.in

Chi-Won In
Materials and Processes Engineering,
Pratt and Whitney,
East Hartford, CT 06118
e-mail: chi-won.in@prattwhitney.com

D. A. Raulerson
Materials and Processes Engineering,
Pratt and Whitney,
Jupiter, FL 33478
e-mail: dave.raulerson@prattwhitney.com

Transient vibro-thermography for nondestructive evaluation and super-resolution imaging of material defects invariably employs nonlinear contact dynamics involving the ultrasonic actuator (horn) and the surface of the target structure. It produces nonlinear resonant modes of vibration in the target structural component. Vibration-induced heat generation is one phenomenon involved here. However, the contribution of nonlinear vibration on the thermal signature is poorly understood. In this study, we consider a metallic component with a thin-walled cavity as a representative sharp feature tuned to the main excitation frequency of the ultrasonic actuator. We have developed a mathematical model to simulate transient thermal signature of structural discontinuity/cavity/defect. The model incorporates a coupled thermo-viscoelastic heat generation process in the bulk material based on the Helmholtz free energy formulation. To capture the source of nonlinear resonant modes, we incorporate the stick-separation contact dynamics due to the ultrasonic horn and the target structural component. Commercial finite element simulation (COMSOL MULTIPHYSICS) is used to quantitatively understand the nonlinear vibration response and the thermal transport behavior of the target structure with the cavity. The proposed model accounts for the effects of both the normal and the shear components of deformation contributing on heat generation and captures the nonlinear modal contribution on the heat flux map. The study shows how the geometric feature and material parameters produce an evolution of the nonlinear subsuper harmonics along with the primary harmonics tuned to the excitation frequency. Results obtained from numerical simulations are compared with the experimental results. [DOI: 10.1115/1.4046860]

Keywords: transient vibro-thermography, nonlinear, resonant modes, cavity, contact dynamics, Helmholtz free energy, thermoelasticity, modal analysis, nonlinear vibration, ultrasound

1 Introduction

Vibro-thermography is widely used in the nondestructive inspection of structural components, where the target specimen is excited using a contact actuator, and thermal transport is measured using thermal imager [1,2]. Thermoacoustics or thermosonics is one type of the vibro-thermography phenomenon, where a part of high-frequency waves gets converted into thermal energy and its thermal signature can be detected using infrared imagers from the surface of the object [3]. The high-frequency waves are typically generated by acoustic or ultrasonic actuators. The ultrasonic actuators operate in the frequency range of 20–40 kHz, and the central operating frequency is tuned to typically the resonant frequency of the actuator with its booster and a horn for contact at the front side to amplify the input energy to the target structure. The nature of wave energy interaction across the contact surface and into the target structural features and further conversion of the energy into heat energy due to the material damping effect and geometric feature or defect are the most important aspects in the design of the vibro-thermography technique and interpretation of the thermal signature. Heat generation in the region of defects is quite different compared to that of the surrounding bulk material regions with macroscale surfaces relative to the wavelength. The corresponding change in the temperature distribution in the specimen is monitored by an infrared imaging camera [4–6]. This enables the detection and identification of the features or defects of the size, which could be much smaller than the elastic wavelength, which is due to the conversion of wave energy into heat energy at the smaller scales of vibration or in other words due to super-resolution properties. Studies report potential of ultrasonic based transient vibro-thermography to identify defects in a metallic structure including inaccessible corrosion defects [7,8], surface cracks [9], nonuniform thermal barrier coating [10], etc. Delamination of layered media due to the impact of damage and disbond between joints was identified using the vibro-thermography technique at high frequency [11–13]. This technique shows promising results in detecting such defects; however, the accuracy and the reliability behind its potential capability have remained questionable.

Besides, numerous studies report the potentials of the vibro-thermography technique as a nondestructive evaluation (NDE) technique; however, the heat generation process during this phenomenon in the bulk of the material is not well reported. Different hypotheses have been suggested in different studies. For example, Farren and Taylor [14] employed a hardening model to estimate the material plastic state and measured the heat energy developed during the process by estimating the lag in temperature between the thermojunction and the specimen. Mason et al. [15] used a high strain rate model to estimate the thermal softening of the material. Rosakis et al. [16] proposed a model of thermoplastic heating by considering only the plastic part of the strain. Mabrouki et al. [17] developed a numerical scheme for plastic deformation by neglecting elastic deformation to correlate the vibro-thermography test results. The heat generation models to understand the vibro-thermography phenomena discussed earlier are empirically established based on the experimental observations. The models discussed earlier do not consider the contribution of all the components of the strain. They also do not explain whether and when the plastic strain is important compared to any viscous dissipation in the bulk material particularly where the strain magnitude is small due to the high-frequency vibration as in the case of transient vibro-thermography. Therefore, more quantitative and systematic studies using physically consistent modeling and simulation would help to better understand the transient vibro-thermography and be a reliable NDE technique.

[1]Corresponding author.

Contributed by the Design Engineering Division of ASME for publication in the JOURNAL OF VIBRATION AND ACOUSTICS. Manuscript received January 20, 2020; final manuscript received April 2, 2020; published online May 22, 2020. Assoc. Editor: Melih Eriten.

In this study, Helmholtz free energy-based formulation is employed to understand the influence of the strain rate components as in full three-dimensional condition onto the heat generation from the resonant cavity. Also, the nonlinear interaction between the ultrasonic actuator horn and the target structure is captured. Hence, we use a stick-separation contact dynamics model and simulate the evolution of the nonlinear response in terms of nonstationary ultrasonic wave modes and the resulting thermal energy localization in the cavity.

2 Mathematical Model and Simulation Scheme

The simulation scheme incorporates (a) a coupled thermo-viscoelastic model of heat generation derived consistently based on Helmholtz free energy formulation and (b) a stick-separation contact dynamics model to capture the evolution of nonlinear phenomena during vibro-thermography. The details of these models are described in Secs. 2.1 and 2.2, respectively. The details of the finite element simulation scheme are discussed in Sec. 2.3.

2.1 Coupled Thermo-Viscoelastic Model

. A recent study [18] in a thick slab with a flat bottom hole assumed that heat generation in the bulk material is entirely only due to the square of the in-plane strain, neglecting other strain components and viscoelastic damping effect. In the present study, we have employed a recently developed a generalized coupled thermo-viscoelastic heat generation model based on the Helmholtz free energy formulation [19]. The formulation naturally includes the contribution of each of the shear strain rates associated with the viscous dissipation and further couples the transient heat transport equation via the heat flux term. We summarize the mathematical details below with reference to further details in Refs. [19,20]. Applying the first law of thermodynamics, the energy conservation equation in rate form can be expressed as follows:

$$\rho\dot{U} = \dot{\varepsilon}_{ij}\sigma_{ij} + \frac{1}{V}\frac{dQ}{dt} = \dot{\varepsilon}_{ij}\sigma_{ij} + r - q_{i,i} \tag{1}$$

where U is the specific internal energy, a state function; ρ, V, q_i, and r are the density, volume, heat flux vector, and the specific heat energy rate, respectively; σ_{ij} and ε_{ij} are the stress and strain tensors, respectively; and dQ/dt is the total heat energy input rate. The second law of thermodynamics in the form of Clausius–Duhem inequality gives

$$\rho\dot{s} - \frac{r}{\theta} + \frac{q_{i,i}}{\theta} - \frac{q_i\theta_{,i}}{\theta^2} \geq 0 \tag{2}$$

where s is the specific entropy, a state function, and θ is the absolute temperature. From Eqs. (1) and (2),

$$\rho\theta\dot{s} - \rho\dot{U} + \dot{\varepsilon}_{ij}\sigma_{ij} - \frac{q_i\theta_{,i}}{\theta} \geq 0 \tag{3}$$

The state functions specific internal energy (U) and specific entropy (s) from the first and second law of thermodynamics, respectively, are expressed in terms of another state function called Helmholtz free energy (ψ) as follows:

$$\psi = U - s\theta \Rightarrow \dot{U} = \dot{\psi} + \dot{s}\theta + s\dot{\theta} \tag{4}$$

The Helmholtz free energy can be expressed using the physical properties and constitutive law for a general inelastic material as follows:

$$\psi = \psi(\theta, \varepsilon_{ij} - \varepsilon^{ie}_{ij}); \quad \rho\frac{\partial\psi}{\partial\varepsilon_{ij}} = \sigma_{ij} - \sigma^{v}_{ij}; \quad \frac{\partial\psi}{\partial\theta} = -s \tag{5}$$

where ε^{ie}_{ij} is the inelastic part of the strain tensor and σ^{v}_{ij} is the viscous stress. The viscous part of the stress can be approximated in a constitute law as follows:

$$\sigma^{v}_{ij} = \mu_{ij}\dot{\varepsilon}_{ij} \tag{6}$$

where μ_{ij} and $\dot{\varepsilon}_{ij}$ are the coefficient of viscosity tensor and strain rate, respectively. For a body that is assumed to be in the homogenous state of deformation, $dQ/dt = \rho C_p\dot{\theta}$, $\sigma^{v}_{ij} = 0$, implies strain rate $\dot{\varepsilon}_{ij} = 0$. C_p is the specific heat at constant strain. Substituting Eqs. (4)–(6) in Eq. (3) and on further simplification gives $-\theta\frac{\partial^2\psi}{\partial\theta^2} = C_p$.

Fourier's law of heat conduction gives the heat flux as follows:

$$q_i = -k_{ij}\theta_{,j} \tag{7}$$

Substituting Eqs. (4), (5), and (7) in Eq. (3) gives

$$\rho C_p\dot{\theta} = (K_{ij}\theta_j)_{,i} + \rho\theta\frac{\partial^2\psi}{\partial\varepsilon_{ij}\partial\theta}(\dot{\varepsilon}_{ij} - \dot{\varepsilon}^{ie}_{ij}) + (\sigma_{ij} - \sigma^{v}_{ij})\dot{\varepsilon}^{ie}_{ij} + \sigma^{v}_{ij}\dot{\varepsilon}^{ie}_{ij} \tag{8}$$

For a thermo-viscoelastic material, by expanding the Helmholtz free energy $\psi(\theta, \varepsilon_{ij})$ in the Taylor series about a reference state ($\theta = \theta_0$) gives

$$\sigma_{ij} = D_{ijkl}(\varepsilon_{kl} - \varepsilon_{0kl}) \tag{9}$$

where $D_{ijkl} = \rho(\partial^2\psi/\partial\varepsilon_{ij}\partial\varepsilon_{kl})$, $\varepsilon_{0kl} = \alpha_{ij}(\theta - \theta_0)$, $\alpha_{ij} = C_{ijkl}\beta_{kl}$, and $\beta_{ij} = -\rho(\partial^2\psi/\partial\varepsilon_{ij}\partial\theta)_0$. The subscript notation $(\,)_0$ denotes the reference state. Substituting Eqs. (6) and (9) in Eq. (8) and assuming isotropic materials gives a coupled thermo-viscoelastic equation:

$$\rho C_p\dot{\theta} = \nabla(k\nabla\theta) - 3B\alpha T(\dot{\varepsilon}_{ii}) + \mu_{\perp}(\dot{\varepsilon}^2_{11} + \dot{\varepsilon}^2_{22} + \dot{\varepsilon}^2_{33}) + 2\mu_{||}(\dot{\varepsilon}^2_{12} + \dot{\varepsilon}^2_{23} + \dot{\varepsilon}^2_{13}) \tag{10}$$

where B and α represents the elastic bulk modulus and coefficient of thermal expansion, respectively. $\mu_{\perp}$ and $\mu_{||}$ are the normal and the shear components of viscosity coefficient tensor, respectively. These coefficients are estimated by fitting an analytical model with the experimental data obtained from a dynamic mechanical test with the material specimen taken from the target structure [21]. A lumped model of the standard linear viscoelastic solid is used [22]. The terms $\mu_{\perp}(\dot{\varepsilon}^2_{11} + \dot{\varepsilon}^2_{22} + \dot{\varepsilon}^2_{33})$ and $\mu_{||}(\dot{\varepsilon}^2_{12} + \dot{\varepsilon}^2_{23} + \dot{\varepsilon}^2_{13})$ are the normal and shear strain rate terms, respectively, which contribute toward the heat generation in the bulk of material. This nonlinear model correlates the effect of in-plane and out-of-plane components with the modes of heat generation.

2.2 Contact Dynamics Model. The literature has reported various possible mechanisms responsible for the nonlinear harmonics like subharmonics, super-harmonics, subsuper-harmonics, and chaos, which may appear due to contact dynamics. Significant effort and advancement have been made to understand the phenomena involving a tuned single-frequency excitation. The contact dynamic phenomenon is highly sensitive to different parameters of actuation by horn contact on the target structure such as excitation frequency relative to the resonance spectral characteristic of the contact-free target component, the amplitude of excitation, engagement force or static preload applied by the actuator horn at the contact interface, and various other parameters related to mechanical boundary conditions [23–26]. In our finite element simulation scheme, we model the vibrating part of the actuator at the contact region or the horn as an elastic cylinder assuming that its own thermal signature does not interfere with that of the target structure, particularly in the cavity region during transient thermal signature measurement. The length of the horn is chosen according to the frequency or wavelength requirement with reference to the resonance spectral characteristics of the contact-free target structure and the size effect due to the feature or the cavity considered in the present problem. Details regarding this aspect of frequency or wavelength tuning have been discussed in our previous study [19]. We model the target structure under the contact region entirely as a full 3D thermo-

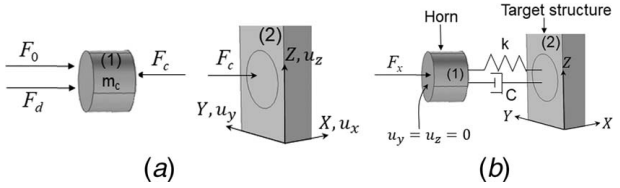

Fig. 1 (*a*) Free-body diagram of the ultrasonic actuator horn end segment and the target structure at the contact interface and (*b*) contact gap with the coupling layer modeled with spring damper in the contact model

viscoelastic domain along with the appropriate mechanical and thermal boundary conditions. The target structure is rigidly mounted on a fixture. The high-frequency resonant mode shapes of the target structure without the horn contact are captured accurately with the help of optimal mesh discretization and time integration of the governing equations. This is to ensure that the strain rate-dependent source terms for heat generation patterns are obtained accurately. However, most of the studies reported in the literature have considered lumped mass approximation. Han et al. [27] and Zheng et al. [28] used lumped mass models to understand the contact impact mechanism between the horn and the target. The aforementioned lumped mass modeling scheme cannot predict the vibration behavior of the target structure accurately because the different resonant mode shape-induced deformations of the target surface make the contact interface non-uniform, and this effect cannot be modeled by lumped mass approximation. Such a model mainly captures the dynamic contact interaction assuming flat surfaces and ignores the material and geometry effects of the source and the target. Moreover, the results reported are sensitive to only the initial velocity and no other parameters and spatial points of measurement, and therefore a better model needs to be used.

During vibro-thermography, the ultrasonic actuator horn is excited using a single-frequency sinusoidal signal along with a static preload or engagement force [24]. The initial deformation due to the engagement force compresses the contact interface, and this state becomes the reference state before the transient vibration starts due to horn excitation. If the resonant effect of the target surface is ignored, a first approximation is that the horn will remain in contact with the target structure during the compressive part of the excitation cycle (stick condition) and will separate from the target structure somewhere during the retraction cycle (separation condition). Switching between these two states is via a nonlinear change in the forcing condition. We further assume that the actuator delivers the required force against the reaction from the target surface, and it also follows the displacement profile under no force as in the case of contact-free motion of the horn. In summary, this is the main feature of the contact dynamics model we have considered here. In our experiments, a coupling material is introduced between the ultrasonic horn and the target

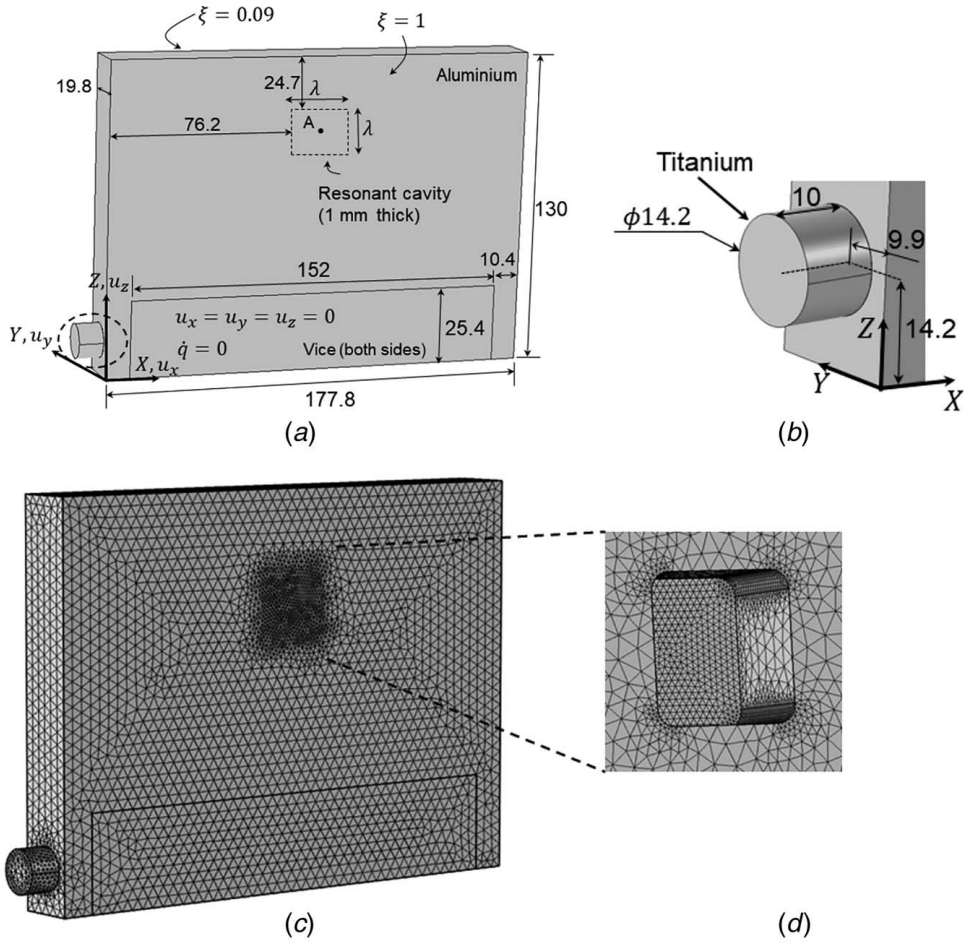

Fig. 2 Schematic illustrates an ultrasonic horn and a metallic component with the cavity used for the transient vibro-thermographic simulation. (*a*) Dimensions of the target structure and (*b*) the actuator used in the simulation. All dimensions are represented in mm. (*c*) Isometric and (*d*) enlarged backside view of finite element meshes used for simulation.

Table 1 The values of various parameters used in the simulation

Parameters	Values
Engagement or static force (F_0)	266.8 N
Mass of cylinder (segment of horn) (m_c)	0.0078 kg
Mass of horn (m_H)	0.1026 kg
Excitation frequency (f_{exc})	30 kHz
Coefficient of convective heat transfer (h)	25 W/(m^{2}K)
Stefan–Boltzmann constant (σ)	5.670367×10^{-8} (W m^{-2} K^{-4})
Normal coefficient of viscosity	170.3 Pa·s
Shear coefficient of viscosity	64.02 Pa·s

structure to eliminate surface ablation of the target structure [29]. As explained earlier, the end segment of the actuator horn is modeled as an elastic cylindrical with mass (m_c) (see Fig. 1). The inertial effect of the remaining segment (mass m_H) of the horn is introduced through an equivalent dynamic force:

$$F_d = (m_H - m_c)u_0\omega^2 \sin(\omega t) \tag{11}$$

which ensures the driven displacement profile in the contact-free condition, where u_0 is the displacement amplitude of the input port at the backside cut surface of the horn segment modeled as a cylinder and ω is the excitation frequency in rad/s. The effective axial force $F_x = F_d + F_0$, where F_0 is the engagement force (see Fig. 1(*a*)). The stick-separation contact constraints are given as follows.

Case 1: During the compression part of the cycle, to restrict the horn from impinging on the target surface, a multipoint constraint condition over the contacting surfaces is applied to enforce displacement continuity, that is, if $u_x^{(1)} \geq u_x^{(2)}$ applied constrain:

$$u_x^{(1)} = u_x^{(2)} \tag{12}$$

where $u_x^{(1)}$ and $u_x^{(2)}$ are the displacements of the horn surface and target surface, respectively.

Case 2: During the retraction or separation part of the cycle, the contact force (F_c) on both the faces of the contact region (horn and target surfaces) is due to the coupling material, that is,

$$F_c = k(u_x^{(2)} - u_x^{(1)}) + C(\dot{u}_x^{(2)} - \dot{u}_x^{(1)}) \quad \text{if } |u_x^{(2)} - u_x^{(1)}| \leq h_c$$

$$F_c = 0 \quad \text{if } |u_x^{(2)} - u_x^{(1)}| > h_c \tag{13}$$

where h_c, k, and C are the thickness, stiffness, and the damping of the coupling material. The free-body diagram at the contact interface is shown in Fig. 1(*a*). The effect of the coupling material is not the focus of the current study, and hence, the effect of the coupling material is neglected in the simulation. The surface of the actuator horn is shown in Fig. 1(*b*) is constrained in the lateral directions ($u_y = u_z = 0$) to eliminate the problems of rigid body motion in the lateral directions. Here, we also assume that the transient contact dynamics does not produce traveling wave that travels along the length of the horn and reflect to the contact region leading to additional effects. We also assume that the work done by the horn is within the saturation limit of the power delivered by the actuator and the actuator is stiff enough to produce the required force. The developed model takes care of the nonlinear vibration phenomenon, which is highly sensitive to excitation parameters such as excitation intensity, frequency, and engagement force. The nonlinear evolution of the thermal signature is highly nontrivial and complex and needs to be analyzed with the help of simulated and experimental data in order to understand the role of the individual resonant mode shapes.

2.3 Simulation Scheme. We implemented the aforementioned mathematical model in the commercial finite element software

Table 2 Eigen frequencies in the frequency ranges of 1–10 kHz, 20–35 kHz, and 58–70 kHz are shown in columns 2, 3, and 4, respectively

Sl. No	Eigen frequencies (kHz) (1–10 kHz)	Eigen frequencies (kHz) (20–35 kHz)	Eigen frequencies (kHz) (58–68 kHz)
1	1.670	20.319	58.719
2	2.543	21.109	58.887
3	4.890	22.532	59.280
4	5.781	22.561	59.705
5	8.819	23.334	60.218
6	8.845	24.739	60.749
7	–	25.272	61.006
8	–	25.318	61.177
9	–	25.408	61.868
10	–	26.644	62.016
11	–	28.902	62.037
12	–	29.040	62.422
13	–	30.531	63.409
14	–	31.004	63.951
15	–	31.037	63.980
16	–	31.1142	64.059
17	–	31.704	65.447
18	–	33.458	65.978
19	–	34.142	66.115
20	–	–	66.447
21	–	–	67.074
22	–	–	68.022
23	–	–	68.382
24	–	–	69.055
25	–	–	69.181
26	–	–	69.515
27	–	–	69.582

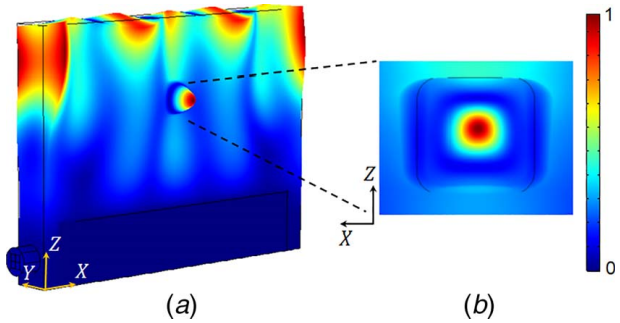

Fig. 3 Normalized resultant displacement mode shape on (*a*) the surface of the target structure and (*b*) the backside wall with normal zoomed view of the cavity at an Eigen frequency of 30.531 kHz

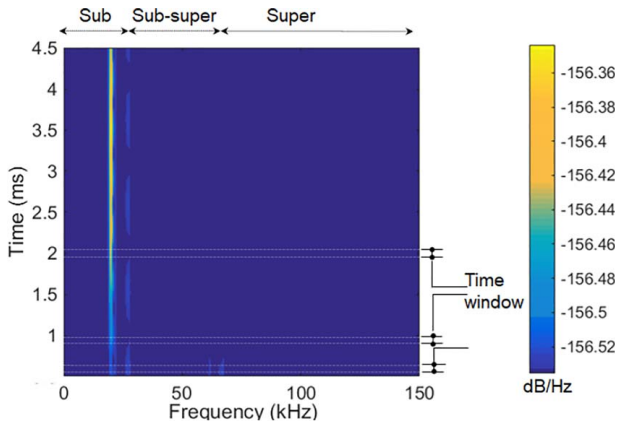

Fig. 4 Spectrogram showing the time–frequency map of surface normal displacement response at point "A," which is located at the center of the resonant cavity sidewall (see Fig. 2(a))

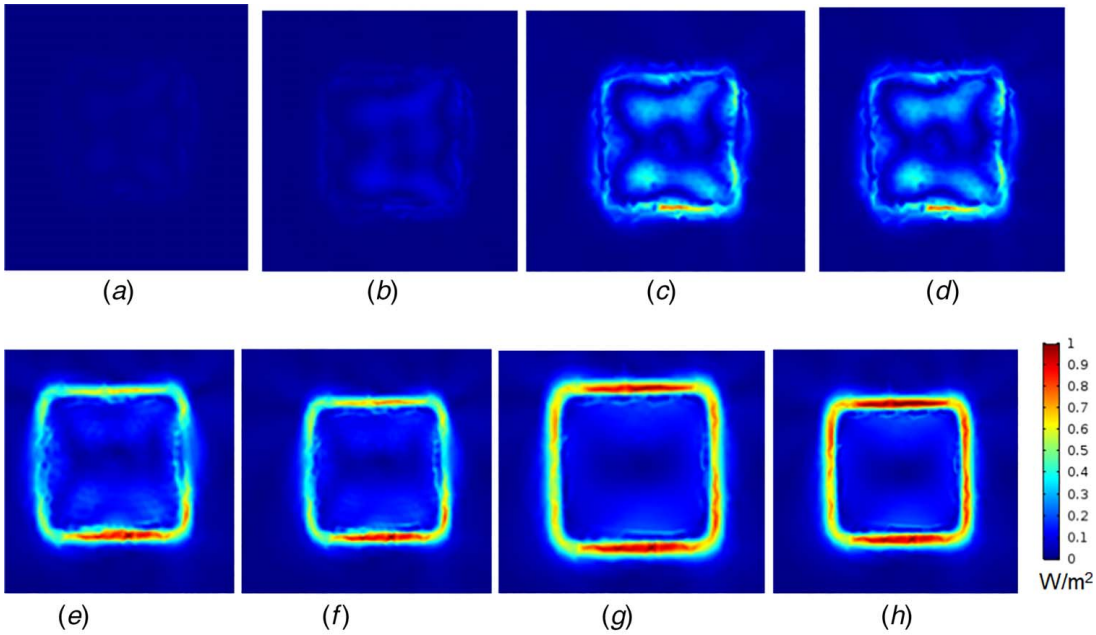

Fig. 5 Spatiotemporal transient surface heat flux map obtained from simulations in the region of cavity at different time stamps: (*a*) 0.1 ms, (*b*) 0.15 ms, (*c*) 0.5 ms, (*d*) 0.9 ms, (*e*) 1.6 ms, (*f*) 2 ms, (*g*) 3.8 ms, and (*h*) 5 ms

COMSOL MULTIPHYSICS. Simulations using the developed model are performed to quantitatively understand the vibration and the thermal transport behavior in the target structure with the resonant cavity. Figure 2(*a*) shows the dimensions of the target structure, which is a thick plate with a cavity. The mechanical and the thermal boundary conditions are as follows: mechanically fixed boundary condition at the base $u_x = u_y = u_z = 0$ and thermal insulation $\dot{q} = 0$ at the base, black body radiation condition $\xi = 1$ on the front surface, and surface emissivity of $\xi = 0.09$ assuming 6024 Aluminum alloy on rest of the surfaces. The dimensions of the resonant cavity are tuned with respect to excitation frequency and wavelength [19]. On all surfaces except the base region, thermal boundary conditions such as a convective and a radiative heat flux boundary conditions are applied together as follows:

$$\dot{q} = h(\theta - \theta_0) + \xi\sigma(\theta^4 - \theta_0^4) \tag{14}$$

where h is the coefficient of convective heat transfer, σ is the Stefan–Boltzmann constant, and θ_0 is the ambient temperature. For the case of transient finite element simulation, the element size and the time integration step are estimated according to the Courant–Friedrichs–Lewy criteria to obtain a converged solution. The maximum size of the tetrahedral finite element is set to one-

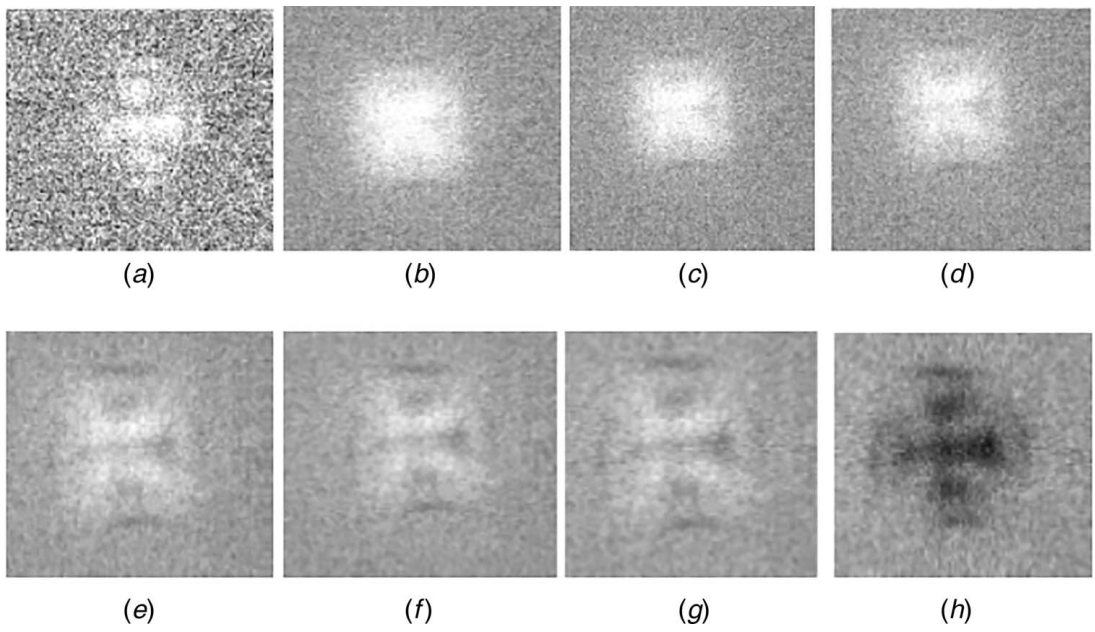

Fig. 6 Spatiotemporal transient thermal transport pattern obtained from experiments in the region of cavity at different time stamps: (*a*) 0.14 s, (*b*) 0.44 s, (*c*) 0.46 s, (*d*) 0.48 s, (*e*) 0.52 s, (*f*) 0.54 s, (*g*) 0.56 s, and (*h*) 0.8 s

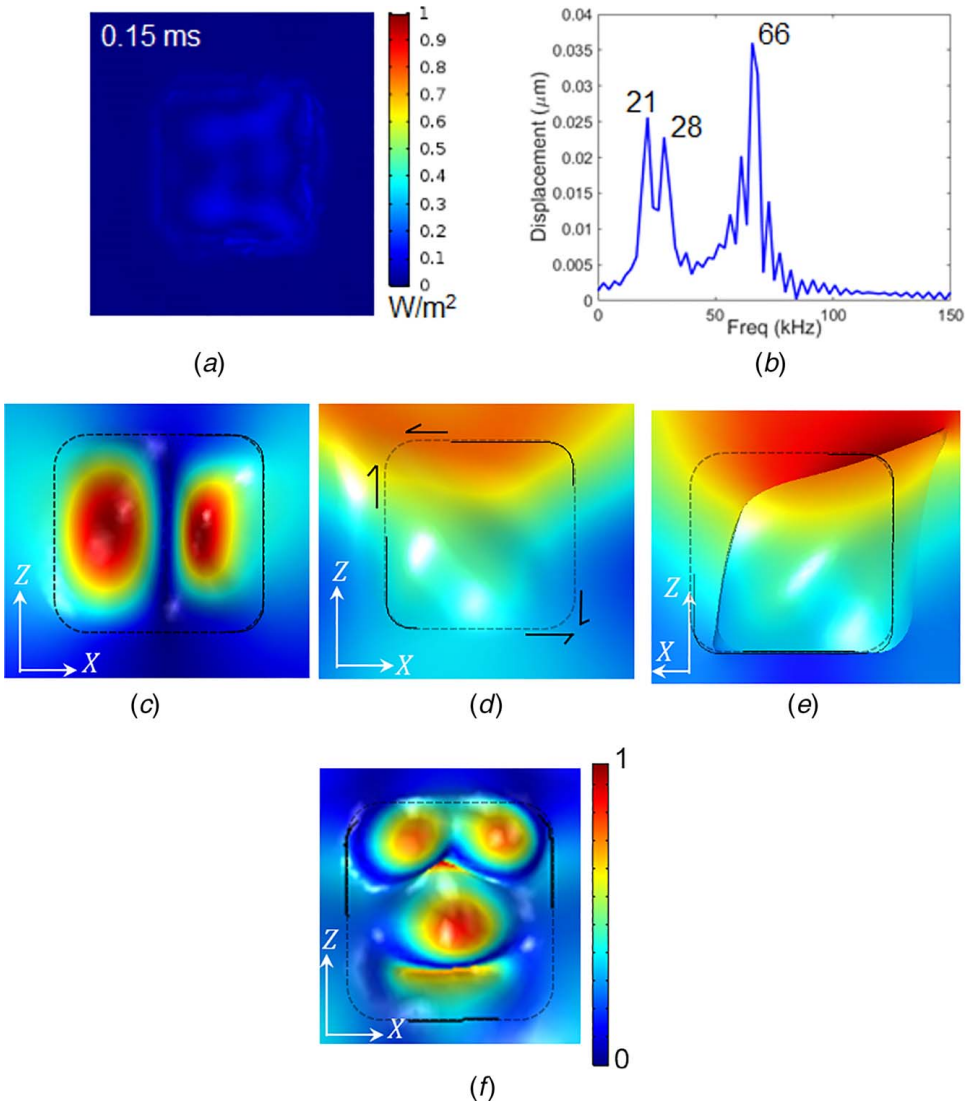

Fig. 7 (*a*) The transient heat flux map obtained from the simulation at 0.15 ms (see Fig. 5(*b*)), (*b*) the frequency spectrum obtained for the time window 0.1–0.3 ms (shown in Fig. 3(*d*)), and (c)–(*f*) the normalized resultant displacement mode shapes obtained in the region of cavity for Eigen frequencies at (c) 21.109 kHz, (*d*) and (e) 28.902 kHz, and (*f*) 66.115 kHz

tenth of the wavelength (λ) of the propagating guided elastic wave in the plate for an excitation frequency of 30 kHz. The finite element mesh used for simulation is shown in Figs. 2(*c*) and 2(*d*). The details of the calculation procedure can be found in the Ref. [30]. The various parameters and corresponding numerical values used in the simulations are given in Table 1.

3 Results and Discussion

In the present study, the dimensions of the cavity (as shown in Fig. 2(*a*)) are tuned using the concept of resonance due to the wavelength scale effect for an excitation frequency of 30 kHz [19]. The method was developed by Nag et al. [31] to identify delamination and estimate its size. That study reported amplification of elastic waves at the delamination, when the delamination dimensions matched with an integral multiple $\lambda/2$. λ can be optimally tuned with the thickness of the structure based on the theory of elastic guided wave propagation (see Refs. [32], [33] and references therein). The literatures has indicated one order higher magnitude of out-of-plane displacement compared to its corresponding in-plane displacement, as the target structures were excited out-of-plane in most cases. In our present study, we consider excitation induced longitudinally at one edge of the thick plate and therefore initial wave modes localized around the excitation region are expected to be predominantly longitudinal. To amplify the out-of-plane vibration in the cavity, the cavity is designed asymmetrically with respect to the mid-plane using the thin sidewall of the cavity, leading to longitudinal flexural–shear coupling around the cavity. The dimensions of the cavity are tuned to its bending or flexural wavelength to obtain a flexural resonance in the cavity. Kolappan Geetha et al. [19] used this concept to maximize the temperature rate in a resonant cavity.

To validate the effectiveness of the chosen dimensions of the cavity based on the aforementioned procedure, an Eigen frequency analysis is performed on the target specimen (as shown in Fig. 2(*a*)). Simulations are performed on the target specimen, where the dimensions of the cavity are tuned with respect to the wavelength ($\lambda = 25.4$ mm) corresponding to the excitation frequency of 30 kHz. Eigen frequencies obtained for different frequency ranges of (i) 1–10 kHz, (ii) 20–35 kHz, and (iii) 58–70 kHz are shown in Table 2. The normalized resultant displacement mode shapes of

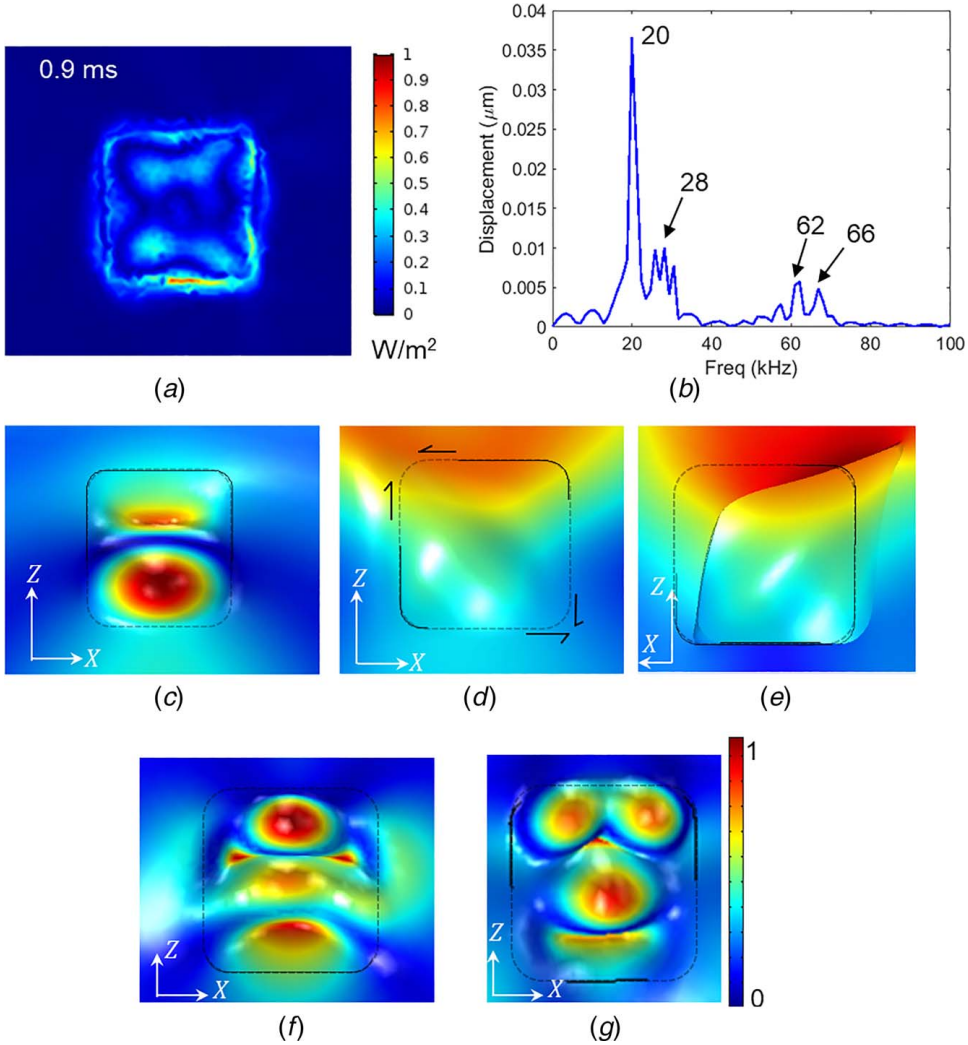

Fig. 8 (*a*) The transient heat flux map obtained from the simulation at 0.9 ms (see Fig. 5(*d*)), (*b*) the frequency spectrum obtained for the time window of 0.8–1 ms (shown in Fig. 3(*d*)), and (c)–(*g*) the normalized resultant displacement mode shapes obtained in the region of cavity for Eigen frequencies at (c) 20.319 kHz, (*d*) and (e) 28.902 kHz, (*f*) 62.037 kHz, and (*g*) 66.115 kHz

the resonant cavity for an Eigen frequency 30.531 kHz are shown in Figs. 3(*a*) and 3(*b*). The Eigen frequency analysis clearly indicates the presence of fundamental flexural resonance mode for the chosen dimensions of the cavity.

The time history and the spectral components analyzed at point "A" (Fig. 2(*a*)) in the cavity are shown using a spectrogram (see Fig. 4). The spectrogram is a time–frequency plot, where the amplitude is represented by the color intensity. The spectrogram in Fig. 4 shows the presence of subsuper-harmonics. There can be three types of harmonics in displacement or velocity spectrum: (a) subharmonics, which are the harmonics of the first kind with frequencies, which are fractions of the excitation frequency; (b) superharmonics, which are the harmonics of the second kind with the frequency of integral multiples of the excitation frequency; and (c) ultra-subharmonics, which are the harmonics of the third kinds, which are kinds of subharmonics but appear in the higher side of the spectrum higher than the excitation frequency. These nonlinearities can exist alone or in a combined form. These nonlinear effects generated in the target structure are highly sensitive to the input energy, location, and magnitude of engagement force applied on the horn and the boundary conditions of the target. In the present study, the nonlinearities introduced during the contact phenomenon gets coupled to the material and geometric effects even when the actuator is sharply tuned for single-frequency excitation (as shown in Fig. 4).

Simulations are performed using the developed model to obtain a spatiotemporal heat flux map in the region of cavity as indicated in Figs. 1 and 3(*a*). The spatiotemporal thermal transport contours obtained from simulations at various instances of time in the region of cavity are shown in Fig. 5. There is a continuous heat exchange between the cavity and the sidewall, where the later acts as a sink (see Fig. 5(*h*)). The total heat capacity (ρC_p) in the specimen remains nearly constant, but the volume in the cavity is far less compared to the surrounding area. In the cavity, there is a continuous heat flux exchange between the adjacent points until a steady state is reached. This is observed as apparent cooling-like phenomenon in the transient heat flux. The spatiotemporal heat flux map gives a detailed insight regarding the transient heat flux in the region of cavity. To compare the simulation results, thermal images are obtained from the aluminum plate with the thin wall cavity using an infrared camera (FLIR SC6700), with a frame rate of 50 frames/s. The sample is black painted on the front surface to achieve emissivity $\xi = 1$ as in simulation. During experiments, the infrared camera is focused on the region of interest (region with a cavity). The raw images obtained directly from infrared camera are postprocessed with thermographic signal

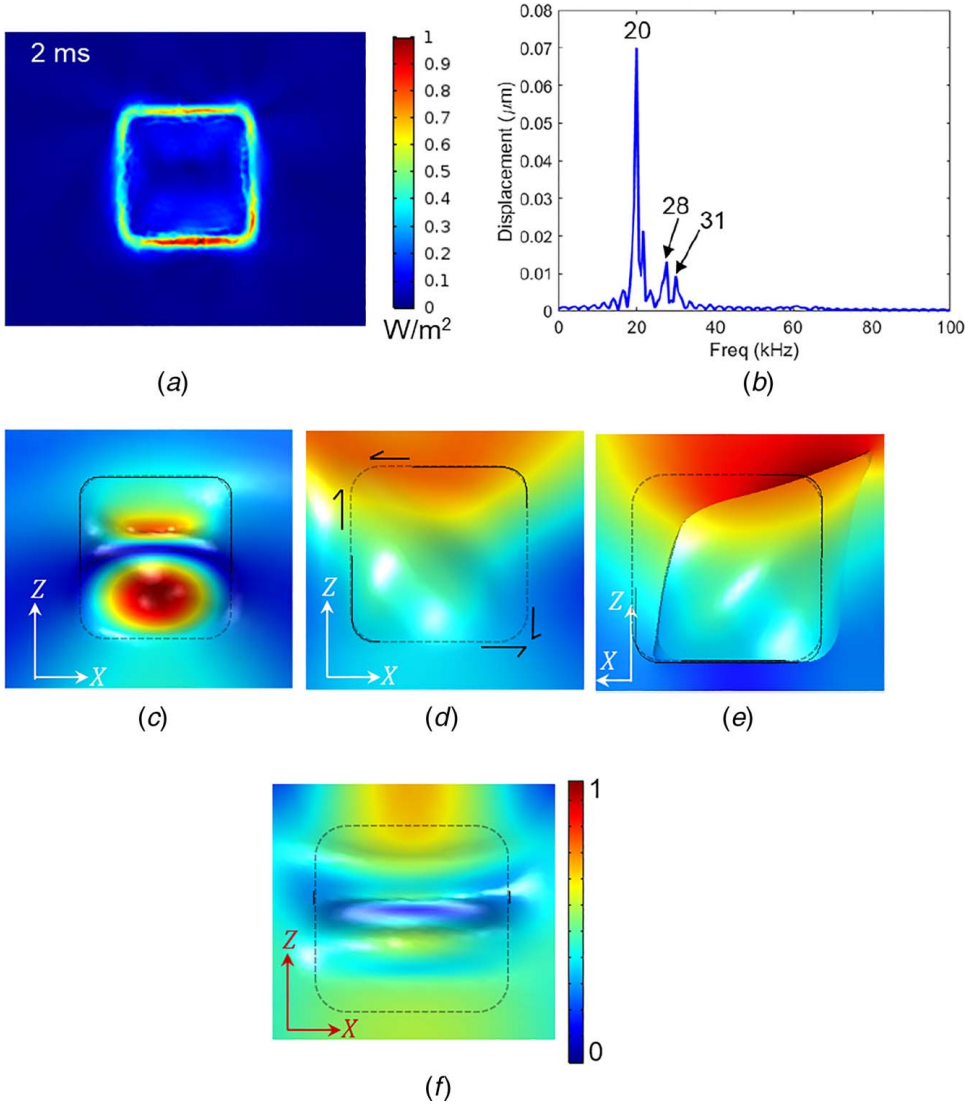

Fig. 9 (*a*) The transient heat flux map obtained from the simulation at 2 ms (see Fig. 5(*f*)), (*b*) The frequency spectrum obtained for the time window 1.9–2.1 ms (shown in Fig. 3(*d*)), and (*c*)–(*f*) the normalized resultant displacement mode shapes obtained in the region of cavity for Eigen frequencies at (c) 20.319 kHz, (*d*) and (*e*) 28.902 kHz, and (*f*) 31.04 kHz

reconstruction (i.e., first derivative image) to provide spatiotemporal thermal transport pattern in the region of interest with a resolution of 640 × 512 pixels. The intensity of the pixel is given in black and white scale in the range of first derivative data. Here, the white region indicates the temperature increase (i.e., positive slope of fitting curve on temperature data) and dark region indicates the temperature drop (i.e., negative slope of fitting curve on temperature data). The spatiotemporal thermal transport contours obtained from the experiment at various instances of time in the region of cavity are shown in Fig. 6. Note that the simulation of vibro-thermography involves high-frequency vibration phenomenon combined with slow thermal transport process. Therefore, the present approach of simulation necessitates time marching for both high-frequency vibration and slow thermal transport simultaneously with fine time-steps, which is time consuming and computationally expensive. Hence, experimental images in Fig. 6 provide only a qualitative comparison of thermal transport contour to the simulation results in Fig. 5.

To better understand the transient heat generation behavior, a correlation with the vibration characteristics is essential. For this purpose, the resonant mode shapes at various Eigen frequencies are simulated and correlated with the thermal transport contour. The time windows corresponding to the transient heat signature at 0.15 ms (Fig. 7(*a*)), 0.9 ms (Fig. 8(*a*)), and 2 ms (Fig. 9(*a*)) are 0.1–0.3 ms, 0.8–1 ms, and 1.9–2.1 ms, respectively (see Fig. 4). The spectral components corresponding to these time windows are shown in Figs. 7(*b*), 8(*b*), and 9(*b*), respectively. Performing spectral analysis at different time windows clearly indicate the presence of other resonant modes or the relative change in the amplitude of the same spectral components. Furthermore, the normalized resultant displacement mode shapes corresponding to the Eigen frequencies are shown in Figs. 7(*c*)–7(*f*), 8(*c*)–8(*g*), and 9(*c*)–9(*f*), and it shows that modal patterns strongly correlate with the thermal transport pattern. The normal and shear strain mode shapes corresponding to these resonance components are shown in Fig. 10. A close observation of the transient heat flux clearly confirms the contribution of the in-plane shear mode shapes (see top-right corner of Fig. 7(*a*)). The resonant mode shape corresponding to 28 kHz depicts an in-plane shear mode in the region of cavity. Vibro-thermographic images show that each resonant mode contributes to the transient heat flux and their superposition in the region of cavity.

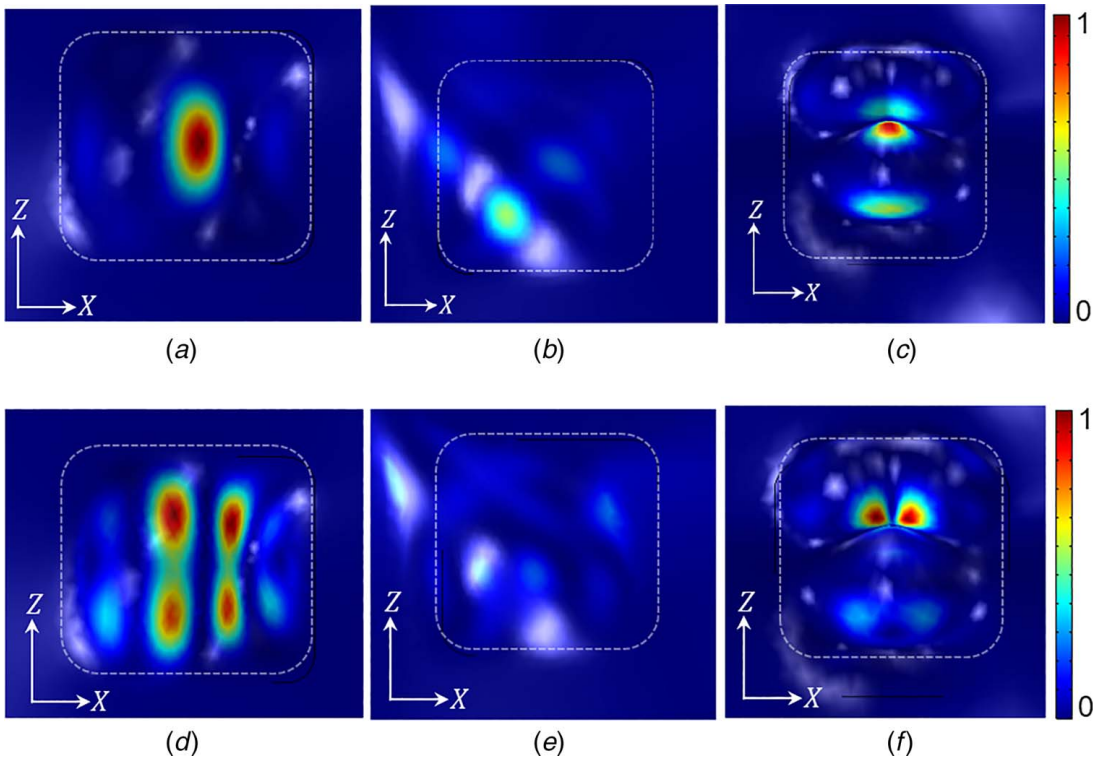

Fig. 10 The normalized axial and shear strain modes obtained in the region of cavity at 21.109 kHz, 28.902 kHz, and 66.115 kHz are shown in (*a*)–(*c*) and (*d*)–(*f*), respectively

4 Conclusion

In this paper, we report the influence of the resonant modes on the thermal signature obtained during transient vibro-thermography. The observations from the simulations and the experiments, involving ultrasound applied to a structure with a resonant cavity, are discussed. The computational model incorporates (i) a thermoelastic coupled heat generation process derived based on the Helmholtz free energy and (ii) the nonlinear stick-separation contact dynamics due to the nonlinear vibration introduced in the ultrasonic horn and the target structure. The thermoelastic model considers the effects of both normal and shear components and can capture the nonlinear modal contribution on the heat flux map. Furthermore, it shows how the nonlinear harmonics-induced spectral characteristics of the horn contact region gets coupled with the specimen with its shape and material effects and those of the cavity via longitudinal flexural–shear wave mode conversion/coupling. The responses are decomposed into modal contributions to understand the heating effect from the strains developed in each mode shape. Some of the resonant modes in the cavity have a strong influence on the thermal signature. A cooling-like modulation phenomenon was observed, which is identified to be due to the continuous exchange of thermal energy across the cavity edges till a steady state is achieved. The results obtained from simulation and experiment provide an insight into the generation of transient heat flux map using superposition from different modal frequencies. The phenomena observed here may find potential application in designing thermoacoustics-based nondestructive imaging.

Acknowledgment

The authors thankfully acknowledge the financial support from Pratt and Whitney, USA (Grant No. 24101) to carry out this research.

References

[1] Pye, C. J., and Adams, R. D., 1981, "Heat Emission From Damaged Composite Materials and Its Use in Nondestructive Testing," J. Phys. D Appl. Phys., **14**(5), pp. 927–941.
[2] Pye, C. J., and Adams, R. D., 1981, "Detection of Damage in Fibre Reinforced Plastics Using Thermal Fields Generated During Resonant Vibration," NDT Int., **14**(3), pp. 111–118.
[3] Mignogna, R. B., Green, R. E., Duke, J. C., Henneke, E. G., and Reifsnider, K. L., 1981, "Thermographic Investigation of High-Power Ultrasonic Heating in Materials," Ultrasonics, **19**(4), pp. 159–163.
[4] Favro, L. D., Han, X., Ouyang, Z., Sun, G., Sui, H., and Thomas, R. L., 2000, "Infrared Imaging of Defects Heated by a Sonic Pulse," Rev. Sci. Instrum., **71**(6), pp. 2418–2421.
[5] Holland, S. D., Uhl, C., Ouyang, Z., Bantel, T., Li, M., Meeker, W. Q., Lively, J., Brasche, L., and Eisenmann, D., 2011, "Quantifying the Vibrothermographic Effect," NDT E Int., **44**(8), pp. 775–782.
[6] Favro, L. D., Thomas, R. L., Han, X., Ouyang, Z., Newaz, G., and Gentile, D., 2001, "Sonic Infrared Imaging of Fatigue Cracks," Int. J. Fatigue, **23**, pp. 471–476.
[7] Busse, G., Wu, D., and Karpen, W., 1992, "Thermal Wave Imaging With Phase Sensitive Modulated Thermography," J. Appl. Phys., **71**(8), pp. 3962–3965.
[8] Zweschper, T., Dillenz, A., and Busse, G., 2001, "Ultrasound Lock-In Thermography—A Defect-Selective NDT Method for the Inspection of Aerospace Components," Insight NDT Condition Monit, **43**(3), pp. 173–179.
[9] Han, X., Favro, L. D., Ouyang, Z., and Thomas, R. L., 2002, "Recent Developments in Thermosonic Crack Detection," AIP Conference Proceedings, Brunswick, ME, July 29–Aug. 3, pp. 552–557.
[10] Wu, D., Zenzinger, G., Karpen, W., and Busse, G., 1996, "Nondestructive Inspection of Turbine Blades With Lock-In Thermography," Mater. Sci. Forum, **210–213**, pp. 289–294.
[11] Zweschper, T., Dillenz, A., Riegert, G., Scherling, D., and Busse, G., 2003, "Ultrasound Excited Thermography Using Frequency Modulated Elastic Waves," Insight NDT Condition Monit., **45**(3), pp. 178–182.
[12] Rantala, J., Wu, D., and Busse, G., 1996, "Amplitude-Modulated Lock-In Vibrothermography for NDE of Polymers and Composites," Res. Nondestruct. Eval., **7**(4), pp. 215–228.
[13] Genest, A. F., Mabrouki, M. F., Ibarra-Castanedo, C., Grenier, M., Larbi, W. B., Bendada, A. H., and Maldague, X., "Comparison of Thermography Techniques for Inspection of Fiber Metal Laminates," 18th Annual ASNT Research Symposium and Spring Conference, St. Louis, MO, Mar. 16–20, pp. 50–54.
[14] Farren, W. S., and Taylor, G. I., 1925, "The Heat Developed During Plastic Extension of Metals," Proc. R. Soc. A, **107**(743), pp. 422–451.
[15] Mason, J. J., Rosakis, A. J., and Ravichandran, G., 1994, "On the Strain and Strain Rate Dependence of the Fraction of Plastic Work Converted to Heat:

An Experimental Study Using High Speed Infrared Detectors and the Kolsky Bar," Mech. Mater., **17**(2–3), pp. 135–145.
[16] Rosakis, P., Rosakis, A. J., Ravichandran, G., and Hodowany, J., 2000, "A Thermodynamic Internal Variable Model for the Partition of Plastic Work Into Heat and Stored Energy in Metals," J. Mech. Phys. Solids, **48**(3), pp. 581–607.
[17] Mabrouki, F., Thomas, M., Genest, M., and Fahr, A., 2010, "Numerical Modeling of Vibrothermography Based on Plastic Deformation," NDT E Int., **43**(6), pp. 476–483.
[18] Solodov, I., Derusova, D., and Rahammer, M., 2015, "Thermosonic Chladni Figures for Defect-Selective Imaging," Ultrasonics, **60**, pp. 1–5.
[19] Kolappan Geetha, G., and Roy Mahapatra, D., 2019, "Modeling and Simulation of Vibro-Thermography Including Nonlinear Contact Dynamics of Ultrasonic Actuator," Ultrasonics, **93**, pp. 81–92.
[20] Ottosen, N. S., and Ristinmaa, M., 2005, *The Mechanics of Constitutive Modeling*, Elsevier, New York.
[21] Menard, K. P., 2008, *Dynamic Mechanical Analysis: a Practical Introduction*, CRC Press, Boca Raton, FL.
[22] Roylance, D., 2001, *Engineering Viscoelasticity*, Department of Materials Science and Engineering–Massachusetts Institute of Technology, Cambridge, MA.
[23] Zhang, C.-S., Feng, F.-Z., Min, Q.-X., and Zhu, J.-Z., 2015, "Effect of Engagement Force on Vibration Characteristics and Frictional Heating in Sonic IR Imaging," NDT E Int., **76**, pp. 52–60.
[24] Feng, F., Zhang, C., Min, Q., and Wang, P., 2015, "Effect of Engagement Force on Vibration Characteristics in Sonic IR Imaging," Ultrasonics, **56**, pp. 473–476.
[25] Han, X., Zeng, Z., Li, W., Islam, M. S., Lu, J., Loggins, V., Yitamben, E., Favro, L. D., Newaz, G., and Thomas, R. L., 2004, "Acoustic Chaos for Enhanced Detectability of Cracks by Sonic Infrared Imaging," J. Appl. Phys., **95**(7), pp. 3792–3797.
[26] Han, X., Li, W., Zeng, Z., Favro, L. D., and Thomas, R. L., 2002, "Acoustic Chaos and Sonic Infrared Imaging," Appl. Phys. Lett., **81**(17), pp. 3188–3190.
[27] Han, X., Loggins, V., Zeng, Z., Favro, L. D., and Thomas, R. L., 2004, "Mechanical Model for the Generation of Acoustic Chaos in Sonic Infrared Imaging," Appl. Phys. Lett., **85**(8), pp. 1332–1334.
[28] Zheng, K., Zhang, H., Zhang, S., and Fan, L., 2006, "A Dynamical Model of Subharmonic Generation in Ultrasonic Infrared Thermography," Ultrasonics, **44**, pp. e1343–e1347.
[29] Song, Y., and Han, X., 2012, "Further Study of Coupling Materials on Aluminum Sample Using Sonic IR," AIP Conference Proceedings, Vol. 1430. No. 1., Burlington, VT, July 17–22, pp. 546–551.
[30] Bathe, K.-J., and Bathe, K.-J., 2006, *Finite Element Procedures*, Prentice Hall, NJ.
[31] Nag, A., Roy Mahapatra, D., Gopalakrishnan, S., and Sankar, T. S., 2003, "A Spectral Finite Element With Embedded Delamination for Modeling of Wave Scattering in Composite Beams," Compos. Sci. Technol., **63**(15), pp. 2187–2200.
[32] Geetha, G. K., Roy Mahapatra, D., Gopalakrishnan, S., and Hanagud, S., 2016, "Laser Doppler Imaging of Delamination in a Composite T-Joint With Remotely Located Ultrasonic Actuators," Compos. Struct., **147**, pp. 197–210.
[33] Rose, J. L., 2014, *Ultrasonic Guided Waves in Solid Media*, Cambridge University Press, New York.